



# Micro-nano fiber-assisted active photoacoustic spectroscopy for gas sensing

MENGPENG HU,<sup>1,2</sup>  HUI ZHANG,<sup>1,2</sup> WEIBIAO WANG,<sup>1</sup> AND QIANG WANG<sup>1,2,\*</sup> 

<sup>1</sup>Changchun Institute of Optics, Fine Mechanics and Physics, Chinese Academy of Sciences, Changchun 130033, China

<sup>2</sup>University of Chinese Academy of Sciences, Beijing 100049, China

\*wangqiang@ciomp.ac.cn

**Abstract:** We report on the development of all-fiber active photoacoustic spectroscopy, where active photoacoustic effect is generated by embedding a micro-nano fiber inside a fiber laser resonator to exploit the evanescent field of the high intracavity power. Acetylene detection at 1530.37 nm was selected for gas sensing demonstration. With a small diameter of 1.1  $\mu\text{m}$ , the tapped fiber exploited  $\sim 20\%$  intracavity power for the evanescent-wave photoacoustic excitation, while only introduced a low intrinsic cavity loss of 0.08 dB. Our sensor achieved a minimum detection limit of 1 ppm at an integration time of 10 s, which can be improved to 73 ppb at 1000 s benefited from the high system stability. The sensing dynamic range was determined to be more than five orders. This spectroscopic technique combines fiber laser, photoacoustic spectroscopy, and fiber evanescent-wave absorption to achieve gas sensing with high flexibility, low optical noise, and easy optical alignment. Current limitations were discussed in detail to explore feasible ways to improve the performance in response time, dynamic range and sensitivity.

© 2023 Optica Publishing Group under the terms of the [Optica Open Access Publishing Agreement](#)

## 1. Introduction

Trace gas detection is critically required across a wide range of applications such as food safety [1], combustion process [2], environmental monitoring [3,4] and respiratory analysis [5,6]. Photoacoustic spectroscopy (PAS), characterized with unique features of zero background, high sensitivity, and wide dynamic range, serves as a promising technique for precise gas detection. It relies on the measurement of absorption-induced acoustic wave rather than attenuated laser, yielding negligible scatter noise, scintillation noise or interference fringe [7]. As the PAS signal scales with the excitation laser power [8], PAS sensors also benefit from the development of high-power lasers and power buildup techniques. Recent advancement includes the employment of optical amplifiers to boost the power of tunable seeds [5,9–11], optical cavities for power buildup [4,9,12,13], and the direct utilization of high intracavity power inside a laser resonator [14–18]. Leveraging on the proposed photoacoustic designs can enhance laser power by one to three orders of magnitude, contributing to the state-of-the-art trace gas detection limit down to ppb even sub-ppb level [11,19]. Up to now, most of the reported power-enhanced studies adopted open-path optics. Precise alignment, beam shaping, and spatial filtering are thereby required to minimize the laser-related noise and to optimize the acoustic wave generation efficiency. Besides, extra feedback control instruments are necessary for the configurations with an optical cavity. A tradeoff between the power enhancement performance and the system robustness must be considered, especially for practical field applications.

Micro-nano fibers have recently driven an interest in gas sensing as exquisite tools to perform light-gas interaction [20,21], which provides evanescent waves with a limited penetration into the sample. Micro-nano fiber found its applications in PAS-based sensing. In 2012, Cao et al. proposed evanescent-wave quartz-enhanced photoacoustic spectroscopy (EW-QEPAS) by exploiting the evanescent-field for photoacoustic generation and realized a normalized noise

equivalent absorption (NNEA) coefficient of  $1.96 \times 10^{-6} \text{ W}\cdot\text{cm}^{-1}\cdot\text{Hz}^{-1/2}$  [22]. In 2017, He et al. introduced multi-point gas monitoring to achieve a quasi-distributed QEPAS sensor [23]. This technique soon extended its implementation to the 2- $\mu\text{m}$  region using a single-mode Ge-doped-silica-core fiber and achieved a NNEA coefficient of  $1.44 \times 10^{-8} \text{ W}\cdot\text{cm}^{-1}\cdot\text{Hz}^{-1/2}$  for carbon monoxide sensing [24]. The introduction of evanescent wave simplifies the sensor design by omitting the precise collimating/focusing optics, which further contributes to a small footprint. Moreover, as PAS signal doesn't rely on the long light-gas interaction, a centimeter-long micro-nano fiber is sufficient for effective acoustic wave generation, which leads to simple fabrication and good robustness.

In this work, we propose the use of a micro-nano fiber waveguide to achieve all-fiber active photoacoustic spectroscopy for trace gas sensing. The micro-nano fiber is assembled inside a fiber laser resonator to fully utilize its high intracavity power. Evanescent wave of a short micro-nano fiber stimulates the acoustic waves. The active all-fiber configuration constructs the flexibility of the whole sensor by eliminating the use of any open-path optical alignment. We introduce the fundamental operation scheme to demonstrate the interaction among laser, micro-nano fiber and gas molecules. The sensor performance was evaluated by performing acetylene ( $\text{C}_2\text{H}_2$ ) measurement, as an example, in the C-band. A minimum detection limit (MDL) of 73 ppb was achieved at an integration time of 1000 s, indicating its reliable stability. The possibility of fast response was also investigated.

## 2. Methods and materials

### 2.1. Fiber ring laser

In this work, erbium-doped fiber is used as the gain medium, and the fiber-ring laser can be simplified as a two-level system. The principle of an erbium-doped fiber laser (EDFL) has been well documented in previous study [25]. Here, only a brief description is reintroduced to clarify the nomenclature and abbreviations. It can be described by

$$\begin{cases} \frac{dN_2}{dt} = W_p N_1 - \frac{N_2}{\tau_2} - \frac{\eta_s q}{S\tau_c} (\sigma_e N_2 - \sigma_a N_1) \\ \frac{dq}{dt} = \frac{\eta_s l_a}{\tau_c} [(1+q)\sigma_e N_2 - q\sigma_a N_1] - \frac{\delta}{\tau_c} q \\ N_1 = N_c - N_2 \end{cases} \quad (1)$$

where,  $N_1$  and  $N_2$  are the particle number density of ground state energy level and excited state energy level, respectively;  $N_c$  is the doping concentration of erbium ion in erbium-doped fiber;  $q$  is the number of photons in the ring cavity;  $W_p = \eta_p P_p \sigma_{ap} / S h \nu_p$  is the pumping probability;  $P_p$  is the pumping power;  $h \nu_p$  is the photon energy of the pump light;  $\sigma_{ap}$  is the absorption cross section at the pump wavelength;  $S$  is the area of erbium-doped optical fiber core;  $\eta_p$  and  $\eta_s$  are the overlap factors of pump optical power and signal optical power in the fiber core, respectively;  $\sigma_a$  and  $\sigma_e$  are absorption cross section and emission cross section, respectively;  $\tau_2$  is the lifetime of the ion at the excited state energy level;  $\tau_c$  is the cycle time of the fiber-ring cavity;  $l_a$  is the length of erbium-doped fiber in the fiber-ring cavity;  $\delta$  is the total loss of the loop.

When the loop reaches steady state,  $dq/dt = 0$ . The intracavity laser power  $P$  is proportional to the number of steady state photons  $\bar{q}$ , which can be numerically expressed as

$$P \propto \bar{q} = \frac{A - B\delta}{\delta} \quad (2)$$

where  $A$  and  $B$  are

$$\begin{cases} A = \frac{S\tau_c l_a (W_p \tau_2 \sigma_e - \sigma_a) N_c}{\tau_2 (\sigma_e + \sigma_a)} \\ B = \frac{S\tau_c (1 + W_p \tau_2)}{\eta_s \tau_2 (\sigma_e + \sigma_a)} \end{cases} \quad (3)$$

## 2.2. Micro-nano fiber

A piece of fused taper fiber is used as the micro-nano fiber in this work. Figure 1 depicts its schematic diagram. The taper waist generates the evanescent waves and its field distribution was simulated using the wave optics module of COMSOL Multiphysics. The calculated evanescent wave power ratio in air (Fig. 2(a)) at the taper waist decreases with the fiber diameter. About 25.7% power ratio can be expected when the diameter is 1  $\mu\text{m}$ . It is worth mentioning that, for a sharp transition zone, some laser can be coupled from the fundamental mode into high order modes, which can be blocked by the micro-nano fiber allowing only the single mode guidance [26,27]. Therefore, extra loss of the micro-nano fiber inevitably weakens the acoustic wave generation efficiency. We evaluated the relationship between the power loss and the length of the transition zone (Fig. 2(b)). A longer transition zone leads to a higher transmittance by slowing down its gradient and a 25-mm length theoretically ensures >99% power transmittance (< 0.05 dB transmission loss). Ideal lossless waveguide might be realized with a much longer length, however, at the cost of high fabrication difficulty. With the optimized parameters, a micro-nano tapered fiber (waist diameter, 1.1  $\mu\text{m}$ ; waist length, 20 mm; transition zone length, 26.5 mm) was fabricated by flame brush method. The diameter and the length of the obtained micro-nano fibers were controlled by the flame moving range and the fiber stretching length [28]. Figure 3(a) shows the real-time power transmittance of the tapered fiber during fiber drawing process, and reaches a final transmittance of 98.18% ( $\sim 0.08$  dB). Figure 3(b) shows the scanning electron microscope (SEM) image of the taper waist part of the micro-nano fiber.

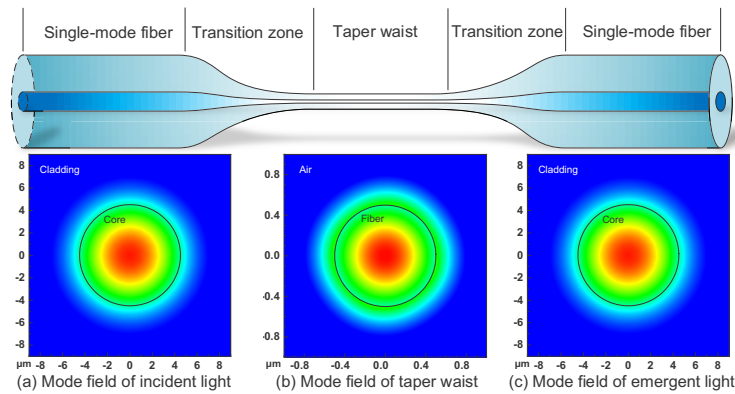


**Fig. 1.** Schematic diagram of the tapered fiber and the simulated mode fields of (a) incident light, (b) taper waist and (c) emergent light.

## 2.3. All-fiber active photoacoustic spectroscopy

At the waist of the tapered fiber, partial power propagates along the surface as evanescent wave, which can be absorbed by the gas when optical frequency is in resonance with the target transition. Absorption induced laser attenuation (in dB) can be expressed as:

$$\delta_g = 10 \times \lg(1 - \eta(1 - e^{-\alpha(v)CL})) \quad (4)$$

where  $\alpha(v)$  is the normalized absorption coefficient,  $\eta$  is the proportion of evanescent wave,  $C$  is the concentration of gas to be measured,  $L$  is the length of the taper waist region.

Combining Eq. (4) and Eq. (2) modifies the intracavity laser power as

$$P(v) \propto \bar{q} = \frac{A - B(\delta_0 - 10 \times \lg(1 - \eta(1 - e^{-\alpha(v)CL}))}{\delta_0 - 10 \times \lg(1 - \eta(1 - e^{-\alpha(v)CL})} \quad (5)$$

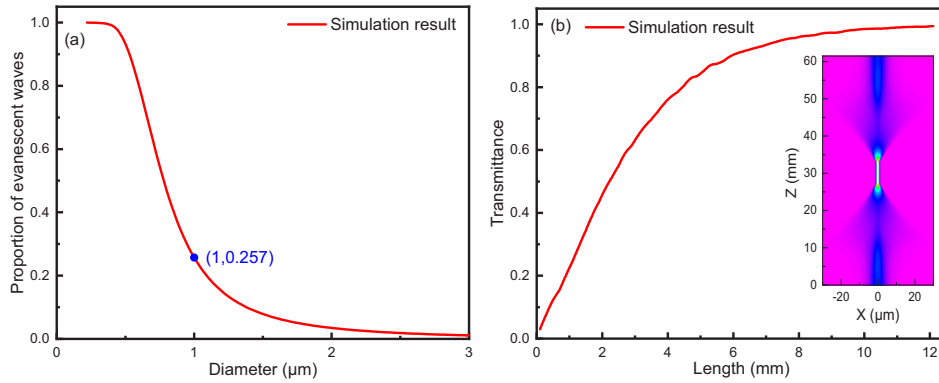


**Fig. 2.** (a) Relationship between evanescent wave energy ratio and taper fiber diameter. (b) Relationship between the power transmittance and the transition zone length. Inset: light propagation in a micro-nano fiber with 25-mm transition zone (direction: from bottom to top).

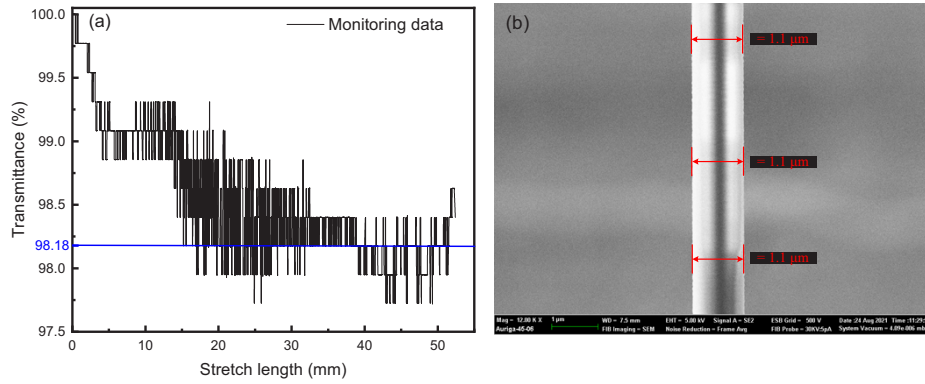


**Fig. 3.** (a) Real-time power transmittance of the tapered fiber during fiber drawing process. (b) Scanning electron microscope (SEM) image of the micro-nano fiber.

where  $\delta_0$  is the intrinsic loss of fiber-ring cavity without gas absorption.  $S_{PAS}(\nu)$ , the photoacoustic signal, scales with gas absorbance of intracavity power  $P(\nu)$  at the frequency  $\nu$  [29,30]:

$$S_{PAS}(\nu) = G\eta P(\nu)(1 - e^{-\alpha(\nu)CL}) \quad (6)$$

where  $G$  is conversion factor between optical signal and acoustic signal. Substituting  $P(\nu)$  in Eq. (5) for that in Eq. (6) produces photoacoustic signal as

$$S_{PAS}(\nu) \propto G\eta(1 - e^{-\alpha(\nu)CL}) \frac{A - B(\delta_0 - 10 \times \lg(1 - \eta(1 - e^{-\alpha(\nu)CL})))}{\delta_0 - 10 \times \lg(1 - \eta(1 - e^{-\alpha(\nu)CL})} \quad (7)$$

Photoacoustic signal can be sensitively retrieved by a lock-in amplifier to perform wavelength modulation spectroscopy. A cosine modulation is applied to the optical frequency of the EDFL,

$$\nu = \nu_0 + \Delta\nu \cos(2\pi f_0 t) \quad (8)$$

and the second harmonic signal is demodulated at  $2f_0$ :

$$S_{2f} = S_{PAS}(\nu) \times \cos(4\pi f_0 t) * F_{low-pass} \quad (9)$$

where  $F_{\text{low-pass}}$  represents transmission function of a low pass filter, the symbol \* represents the convolution algorithm.

The influences of intrinsic cavity loss and micro-nano fiber size on PAS signal were analyzed with system parameters shown in Supplement 1. A higher intrinsic cavity loss can deteriorate the signal amplitude by reducing laser power in resonator (Fig. 4(a)). The sharp dip derives from its approach to the EDFL threshold. Figure 4(b) depicts how taper fiber waist diameter influences the photoacoustic signal at an intrinsic cavity loss of 5 dB. As expected, smaller diameter contributes to better performance by generating acoustic wave with more evanescent power. The system robustness and the fabrication difficulty should also be taken into consideration in practical implementation. 1- $\mu\text{m}$  micro-nano fiber diameter, as a tradeoff, was chosen for our sensor design.

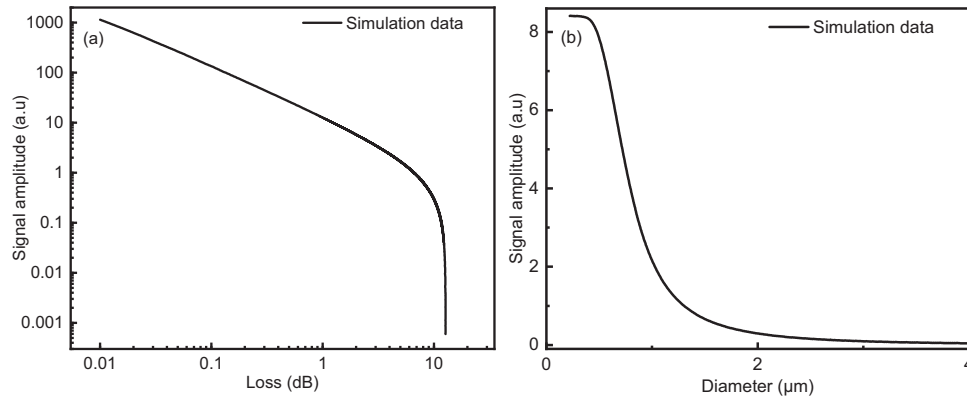


**Fig. 4.** The calculated PAS signal amplitude as a function of (a) intrinsic cavity loss and (b) micro-nano fiber diameter.

### 3. Experimental setup

The schematic of active micro-nano PAS sensor is shown in Fig. 5. The EDFL is pumped by a 980-nm diode laser ( $\sim 830$  mW). Highly erbium-doped silica fiber (EDF) with a length of 1.75 m is used as the gain medium. An optical isolator forces the intracavity laser propagate in a single direction to suppress the noise of back-propagation laser [31]. The fiber Bragg grating (FBG), as a wavelength selector, tunes the EDFL wavelength. A linear tunability is available by applying axial strain to the FBG when coaxially assembled to a piezoelectric actuator (PZT) [32,33]. The home-fabricated micro-nano fiber is inserted into the laser resonator between the FBG and a circulator, enabling enhanced evanescent field by twice propagation through the tapered fiber. The stimulated acoustic wave is then measured by an electret microphone in a PAS cell (Fig. 6). The tapered micro-nano fiber is fixed on two light aluminum blocks using ultraviolet glue. The microphone is located in the middle of a resonance tube (length, 35 mm; diameter, 3 mm; resonant frequency, 4.7 kHz; Q-factor, 3.4). A data acquisition (DAQ) card (USB-6356, NI) acts as the control unit, simultaneously modulating the EDFL wavelength by a piezo driver (PD200, PiezoDrive) and digitizing the PAS signal for the second harmonic demodulation.

Pump laser is guided into the EDF via a WDM. A fiber coupler (coupling ratio: 99:1) shunts 1% laser for intracavity power monitoring and wavelength calibration. The intracavity laser power as a function of the pump power is shown in Fig. 7(a), illustrating a low threshold power of  $\sim 23.6$  mW. The wavelength calibration was performed by a high-speed FBG inquiry analyzer (F2001711, BaySpec) while a 0.1-Hz triangular driving voltage was applied on the PZT. One typical spectrum (Fig. 7(b)) of the EDFL shows a side-mode suppression ratio (SMSR) of 33 dB.

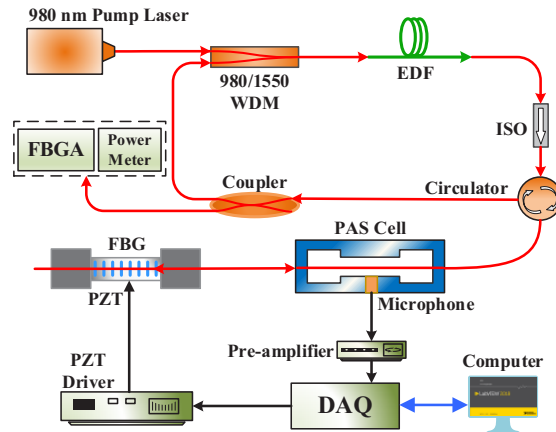


**Fig. 5.** Schematic of the all-fiber active photoacoustic sensor. WDM, wavelength division multiplexer; EDF, erbium doped fiber; ISO: Isolator; FBG, fiber Bragg grating; PZT, piezoelectric actuator; DAQ, data acquisition card; FBGA: FBG inquiry analyzer.

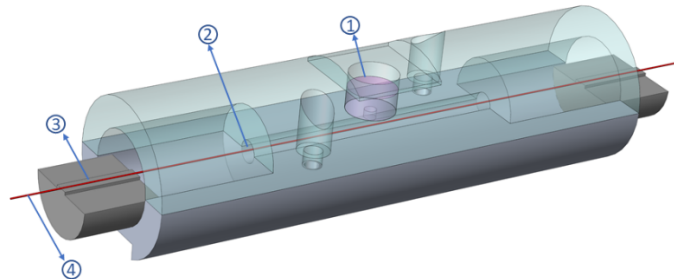


**Fig. 6.** Photoacoustic cell structure. 1. microphone; 2. resonance tube; 3. aluminum block; 4. tapered micro-nano fiber.

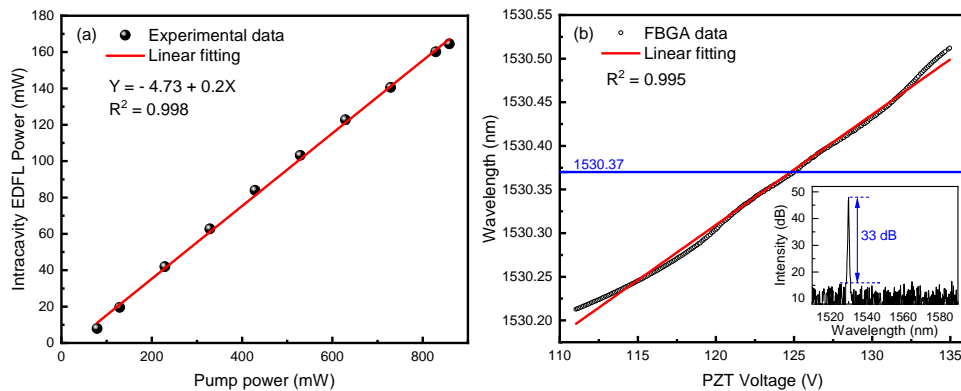


**Fig. 7.** (a) Intracavity laser power as a function of pump power; (b) EDFL wavelength as a function of the voltage applied to the PZT. Inset: typical spectrum of the EDFL.

## 4. Experimental results and discussions

### 4.1. Optimization of modulation voltage and gas pressure

The PAS-2f signal depends on modulation depth of the pump laser [34], which was experimentally evaluated with 1000-ppm  $C_2H_2/N_2$  mixture filled in the PAS cell. The PAS signals were measured by varying the cosine modulation applied on the PZT from 2 to 12 V. Figure 8(a) shows the normalized PAS signal as a function of PZT modulation voltage under different gas pressures (100–1010 hPa). Figure 8(b) shows typical 2f spectra under different pressures at a fixed modulation voltage. The optimized operation gas pressure of 1010 hPa and a PZT modulation voltage of 10 V were therefore chosen for the following experimental investigation.

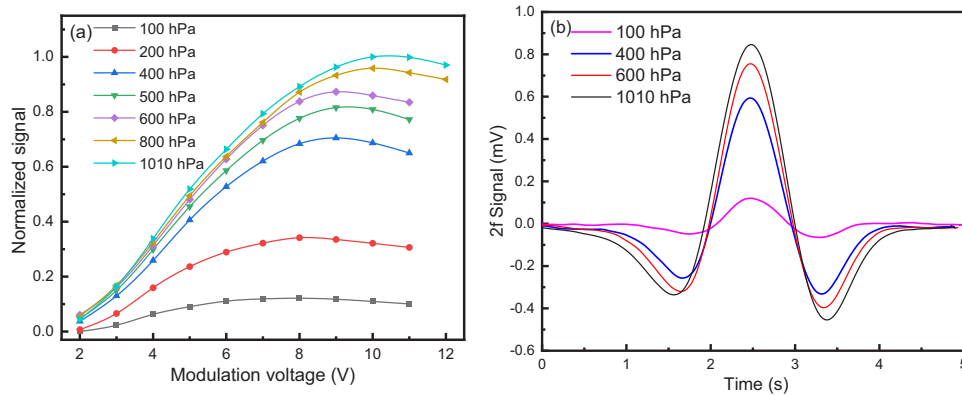


**Fig. 8.** (a) Normalized PAS signals as a function of PZT modulation voltage under different gas pressures; (b) Typical original 2f-spectra under different pressures and a modulation voltage of 10 V.

### 4.2. Sensor performance assessment

With the operation gas pressure and PZT modulation voltage optimized, we further investigated the linearity and stability of the PAS  $C_2H_2$  sensor. A 0.1-Hz triangular signal scanned across the target  $C_2H_2$  absorption line while the wavelength was modulated at 2350 Hz. Different concentrations of  $C_2H_2$  were produced using a commercial gas mixer (Sonimix 7100, LNI Swissgas). The lower  $C_2H_2$  concentration (<1000 ppm) was prepared by diluting the certified 998.6 ppm  $C_2H_2/N_2$  with pure  $N_2$ , while the higher concentration (>1000 ppm) was produced from certified 2.01%  $C_2H_2/N_2$ .

Figure 9(a) shows PAS-2f spectra of samples of 1000 ppm, 80 ppm, and pure  $N_2$ . Figure 9(b) plots PAS-2f amplitude as a function of  $C_2H_2$  concentration, ranging from 30 to 1000 ppm. The linear fitting of the experimental data illustrates a good linear response with an R-square value of 0.9998. Further investigation extended the sample concentration to 10000 ppm (Fig. 9(c)). Obvious nonlinear response is observed mainly due to the fact the absorption at high gas concentration leads to nonnegligible intracavity loss, which is consistent with Eq. (7). Thus, with the absorption-induced cavity loss taken into consideration, fitting based on Eq. (7) can predict the gas concentration with an R-square value better than 0.9999.

Buzzing of the PZT, with the same frequency as the modulation, may perturb the PAS-2f detection as an external noise source. Its impact on the microphone was evaluated by recording the PAS signal with PZT driver alternatively turned on and off (Fig. 10). Potential influence from the gas absorption was avoided with the PAS cell flushed with pure  $N_2$ . The PZT operation brings an extra offset of about 30  $\mu V$ , which remains stable during the sensor implementation. Besides, the variation is slightly increased by 0.4  $\mu V$ . The PZT buzzing influence could be mitigated by

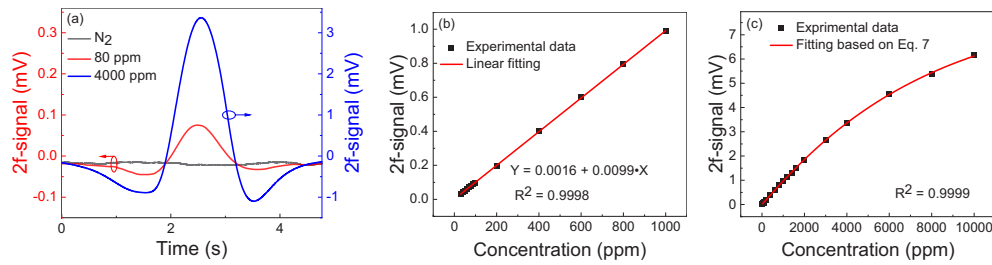


**Fig. 9.** (a) PAS-2f spectra at the concentrations of 80 ppm, 4000 ppm, and pure N<sub>2</sub>; PAS signal as a function of C<sub>2</sub>H<sub>2</sub> concentration, ranging (b) from 30 to 1000 ppm and (c) from 30 to 10000 ppm.

soundproof treatment to the PZT [35] or by designing a differential PAS cell to avoid external common-mode acoustic noise [36].

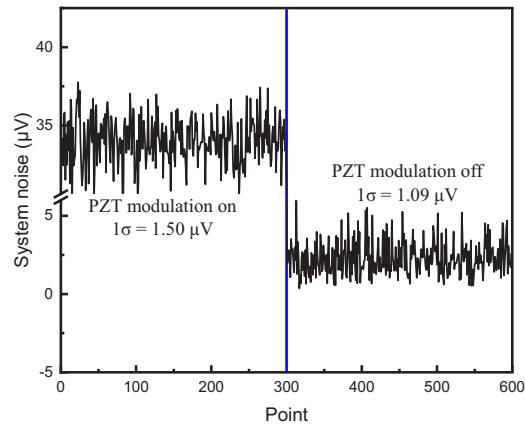


**Fig. 10.** Comparison of the sensor noise when the PZT modulation is switched on and off.

Continuous measurement of PAS signal of pure N<sub>2</sub> was performed to computer the Allan-Variance analysis for the long-term stability assessment. The measurement lasted about 1.5 hours with the analysis results shown in Fig. 11. The Allan-Variance plot shows an MDL of 1 ppm at 10-s integration time and follows a  $1/\sqrt{t}$  dependence until 1000 s, after which instrument drift dominates. The high sensor stability allows averaging without base line or sensitivity drift to improve the MDL down to 73 ppb, corresponding to a noise equivalent absorption coefficient (NEA) of  $8.4 \times 10^{-8} \text{ cm}^{-1}$ . The improved MDL and the highest concentration we employed determine the dynamic range to be about  $1.37 \times 10^5$ .

#### 4.3. Absorption-induced mode hop

By increasing the C<sub>2</sub>H<sub>2</sub> concentration up to 2%, it was of interest to observe the seriously distorted photoacoustic signal. The distortion is attributed to the strong absorption-induced cavity loss, which may disrupt the EDFL operation and detune the wavelength away from the absorption line center. With only scanning voltage applied on the PZT, the EDFL wavelength (black solid curve in Fig. 12) was monitored in real time. The EDFL wavelength deviates from the no-absorption curve (the red dashed curve) from 1530.32 nm. A mode hop occurs at 1530.35 nm, then teleports to 1530.40 nm, which is followed by another deviation until 1530.42 nm. The

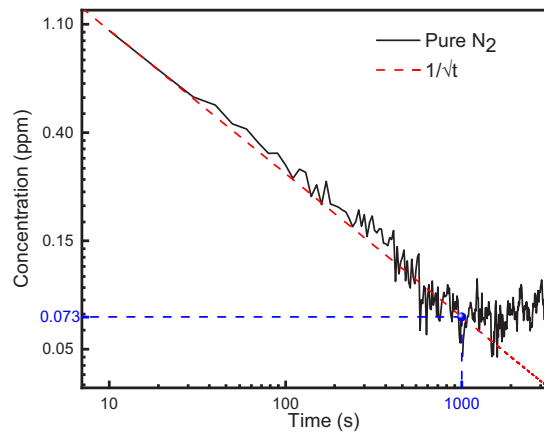


**Fig. 11.** Allan-Variance analysis for pure  $N_2$ .

abnormal wavelength response skips the acetylene absorption region with an absorbance stronger than 0.0233.

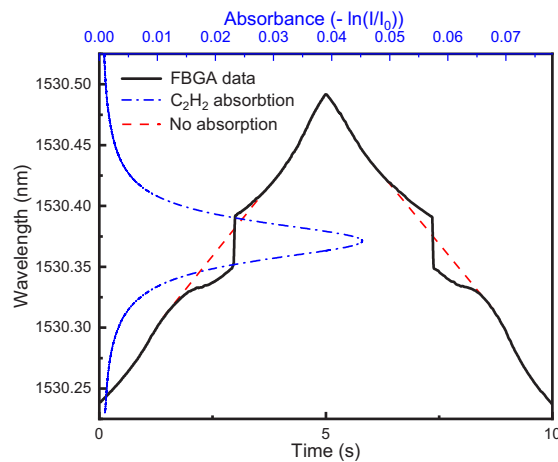


**Fig. 12.** EDFL wavelength response (black curve) with 2%  $C_2H_2$  absorption during PZT scanning. Red dashed curve represents the wavelength without absorption; Blue dotted curve represents 2%  $C_2H_2$  absorption spectrum.

To explain the thick absorption-induced influence on the EDFL operation, an analysis is depicted in Fig. 13. Figure 13(a) shows the reflectance spectrum of the FBG. Figure 13(b) compares the gain curves of 5 selected FBG spectral positions in the case of gas absorption. The solid black curve shows the gain change of point *c* when the PZT-driven FBG scans from 1530.28 nm to 1530.46 nm, in which way  $C_2H_2$  absorption feature is encoded into the intracavity gain. Similarly, the other four gain curves correspond to the four typical points in Fig. 13(a). The point pairs of *a* and *a'*, *b* and *b'* lie symmetrically around the Bragg wavelength (point *c*), and the reflectivity difference between point *a* and *b* equals to that between point *b* and *c*. On the premise that the EDFL usually works at the wavelength with the highest gain within the reflection bandwidth [37], Fig. 13(b) intuitively shows that the EDFL, with 2%  $C_2H_2$  absorption, doesn't always operate at point *c*. The intersection points of these gain curves divide the spectral region into six parts. Region 1 in Fig. 13(b) has the highest gain at point *c* and Regions 2 to 6 have the

highest gain at points  $b$ ,  $a$ ,  $a'$ ,  $b'$  and  $c$ , respectively. Hence, during the PZT-driven FBG scanning with 2%  $C_2H_2$ , the EDFL wavelength follows the gain curves of point  $c$ , then  $b$ ,  $a$ ,  $a'$ ,  $b'$  and  $c$  in sequence (Fig. 13(c), blue dotted curve). In practical EDFL operation, unlike the step changes of these selected points, the gain curve varies continuously along with the absorption profile. Smoothing the blue dotted curve yields distorted EDFL wavelength response to the FBG scanning (Fig. 13(c), black curve), which is consistent with the measured results (Fig. 12, black curve). The mode hop position corresponds to the red intersection point in Fig. 13(b), which is determined by both the thick gas absorption and FBG reflection spectra. A much thinner absorbance by designing a shorter micro-nano fiber could mitigate the absorption-induced mode-hope effect. Then, an extended upper detection limit can also be expected for a wider dynamic range.

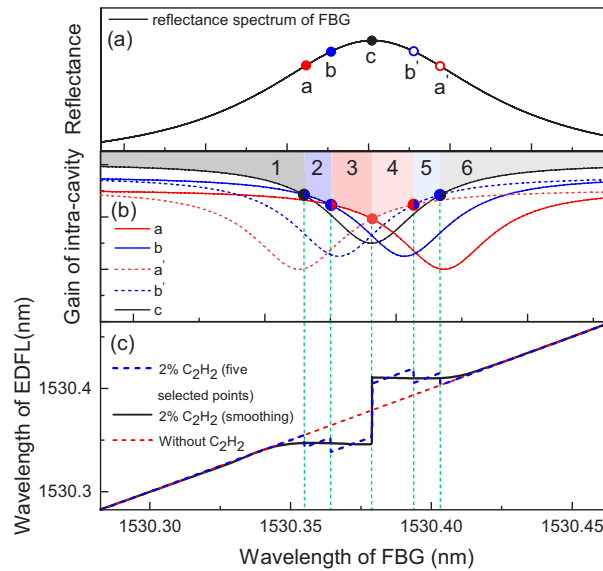


**Fig. 13.** (a) FBG reflectance spectrum; (b) the intra-cavity gain change of example points; (c) the relationship between the EDFL wavelength and the Bragg wavelength.

#### 4.4. Line locking for fast photoacoustic measurement

As the EDFL wavelength may drifts due to the instability of FBG and PZT [38], scanning technique has been performed in the sensing implementation to record the entire absorption profile. The current response is consequently limited to 10 s and is not suitable for the applications that need fast measurement. It is necessary to improve the response time by operating the EDFL at a stable wavelength. We developed a LabVIEW program to implement the third-harmonic ( $3f$ ) method to stabilize the laser wavelength at  $C_2H_2$  absorption line [39,40]. The combination of another reference cell filled with 2%  $C_2H_2/N_2$  and the leaked intracavity laser from the FBG generated the  $3f$ -error signal without changing the sensor configuration. Unlike commonly used current-driven diode lasers, the feedback control was applied on the PZT. Figure 14 compares the long-term recording of PAS-2f signal of 1000-ppm  $C_2H_2$  with the EDFL successively operated in a free running manner and with line locking. Removing the wavelength scanning improves the response time to 1 s. Under the free running mode, the obvious drifts of the PAS-2f signal derives from the instability of FBG, even with a small temperature fluctuation of  $\pm 1^\circ C$  and a negligible strain influence. From 2170 s, the long-term line-locked PAS-2f remains more stable, proving its feasibility for reliable operation by suppressing wavelength fluctuation.

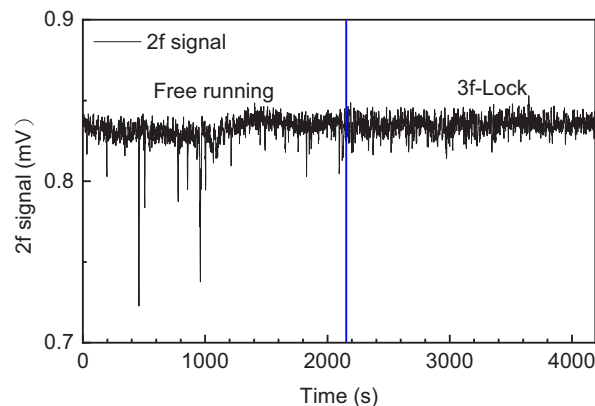


**Fig. 14.** Fast photoacoustic signal measurement with and without locking the laser to the absorption line.

## 5. Conclusion

We have developed all-fiber active photoacoustic spectroscopy and demonstrated its effective ability to detect trace gas concentration. The exploitation of a micro-nano fiber inside a fiber laser resonator generates photoacoustic signal by evanescent wave absorption, which omits the need of any free-space optics for collimation or coupling. By scanning the EDFL wavelength across 1530.37 nm, we have demonstrated a dynamic range of more than 5 orders of magnitude and a minimum detection limit of 1 ppm at 10-s integration time, which can be further reduced to 73 ppb at 1000 s. The response time has been improved to 1 s by locking the EDFL wavelength to absorption line while maintaining a high stability. We also observed the thick absorption-induced mode hop for the first time, which offers an opportunity to extend its upper detection limit by fabricating a much shorter micro-nano fiber. Future research will focus on improving the detection limit by employing a spectrophone with a higher  $Q/f$  ratio, such as a QEPAS acoustic detection module, or by enhancing the local evanescent field with a smaller diameter and a multipass layout in a cascaded manner.

**Funding.** National Natural Science Foundation of China (62005267); Young Talent of Lifting Engineering for Science and Technology in Jilin (QT202106); the Second Comprehensive Scientific Investigation of the Qinghai-Tibet Plateau (2019QZKK020802).

**Disclosures.** The authors declare no conflicts of interest.

**Data availability.** Data underlying the results presented in this paper are not publicly available at this time but may be obtained from the authors upon reasonable request.

**Supplemental document.** See [Supplement 1](#) for supporting content.

## References

1. P. Puligundla, J. Jung, and S. Ko, "Carbon dioxide sensors for intelligent food packaging applications," *Food Control* **25**(1), 328–333 (2012).
2. M. E. Webber, J. Wang, S. T. Sanders, D. S. Baer, and R. K. Hanson, "In situ combustion measurements of CO, CO<sub>2</sub>, H<sub>2</sub>O and temperature using diode laser absorption sensors," *Proc. Combust. Inst.* **28**(1), 407–413 (2000).
3. G. Wysocki, Y. Bakhrkin, S. So, F. K. Tittel, C. J. Hill, R. Q. Yang, and M. P. Fraser, "Dual interband cascade laser based trace-gas sensor for environmental monitoring," *Appl. Opt.* **46**(33), 8202–8210 (2007).
4. A. Rossi, R. Buffa, M. Scotoni, D. Bassi, S. Iannotta, and A. Boschetti, "Optical enhancement of diode laser-photoacoustic trace gas detection by means of external Fabry-Perot cavity," *Appl. Phys. Lett.* **87**(4), 041110 (2005).
5. M. E. Webber, M. Pushkarsky, and C. K. Patel, "Fiber-amplifier-enhanced photoacoustic spectroscopy with near-infrared tunable diode lasers," *Appl. Opt.* **42**(12), 2119–2126 (2003).
6. M. Righettoni, A. Amann, and S. E. Pratsinis, "Breath analysis by nanostructured metal oxides as chemo-resistive gas sensors," *Mater. Today* **18**(3), 163–171 (2015).

7. J. Hodgkinson and R. P. Tatam, "Optical gas sensing: a review," *Meas. Sci. Technol.* **24**(1), 012004 (2013).
8. A. Miklós, P. Hess, and Z. Bozóki, "Application of acoustic resonators in photoacoustic trace gas analysis and metrology," *Rev. Sci. Instrum.* **72**(4), 1937–1955 (2001).
9. R. Bauer, T. Legg, D. Mitchell, G. M. H. Flockhart, G. Stewart, W. Johnstone, and M. Lengden, "Miniaturized Photoacoustic Trace Gas Sensing Using a Raman Fiber Amplifier," *J. Lightwave Technol.* **33**(18), 3773–3780 (2015).
10. Y. F. Ma, Y. He, L. G. Zhang, X. Yu, J. B. Zhang, R. Sun, and F. K. Tittel, "Ultra-high sensitive acetylene detection using quartz-enhanced photoacoustic spectroscopy with a fiber amplified diode laser and a 30.72 kHz quartz tuning fork," *Appl. Phys. Lett.* **110**(3), 031107 (2017).
11. Y. He, Y. Ma, Y. Tong, X. Yu, and F. K. Tittel, "HCN ppt-level detection based on a QEPAS sensor with amplified laser and a miniaturized 3D-printed photoacoustic detection channel," *Opt. Express* **26**(8), 9666–9675 (2018).
12. M. Hippler, C. Mohr, K. A. Keen, and E. D. McNaghten, "Cavity-enhanced resonant photoacoustic spectroscopy with optical feedback cw diode lasers: A novel technique for ultratrace gas analysis and high-resolution spectroscopy," *J. Chem. Phys.* **133**(4), 044308 (2010).
13. S. Borri, P. Patimisco, I. Galli, D. Mazzotti, G. Giusfredi, N. Akikusa, M. Yamanishi, G. Scamarcio, P. De Natale, and V. Spagnolo, "Intracavity quartz-enhanced photoacoustic sensor," *Appl. Phys. Lett.* **104**(9), 091114 (2014).
14. F. P. Wang, Q. S. Xue, J. Chang, Z. L. Wang, J. C. Sun, X. N. Luan, and C. Li, "Wavelength scanning Q-switched fiber-ring laser intra-cavity QEPAS using a standard 32.76 kHz quartz tuning fork for acetylene detection," *Opt. Laser Technol.* **134**, 106612 (2021).
15. Q. Wang, Z. Wang, J. Chang, and W. Ren, "Fiber-ring laser-based intracavity photoacoustic spectroscopy for trace gas sensing," *Opt. Lett.* **42**(11), 2114–2117 (2017).
16. L. Yu, T. G. Liu, K. Liu, J. F. Jiang, L. Zhang, Y. W. Jia, and T. Wang, "Development of an intra-cavity gas detection system based on L-band erbium-doped fiber ring laser," *Sens. Actuators, B* **193**, 356–362 (2014).
17. Q. Wang, Z. Wang, W. Ren, P. Patimisco, A. Sampaolo, and V. Spagnolo, "Fiber-ring laser intracavity QEPAS gas sensor using a 7.2 kHz quartz tuning fork," *Sens. Actuators, B* **268**, 512–518 (2018).
18. Y. Pan, L. Dong, H. Wu, W. Ma, L. Zhang, W. Yin, L. Xiao, S. Jia, and F. K. Tittel, "Cavity-enhanced photoacoustic sensor based on a whispering-gallery-mode diode laser," *Atmos. Meas. Tech.* **12**(3), 1905–1911 (2019).
19. Z. Wang, Q. Wang, H. Zhang, S. Borri, I. Galli, A. Sampaolo, P. Patimisco, V. L. Spagnolo, P. De Natale, and W. Ren, "Doubly resonant sub-ppt photoacoustic gas detection with eight decades dynamic range," *Photoacoustics* **27**, 100387 (2022).
20. Y. Qi, Y. Zhao, H. H. Bao, W. Jin, and H. L. Ho, "Nanofiber enhanced stimulated Raman spectroscopy for ultra-fast, ultra-sensitive hydrogen detection with ultra-wide dynamic range," *Optica* **6**(5), 570–576 (2019).
21. F. Yang, F. Gyger, A. Godet, J. Chrétien, L. Zhang, M. Pang, J.-C. Beugnot, and L. Thévenaz, "Large evanescently-induced Brillouin scattering at the surrounding of a nanofibre," *Nat. Commun.* **13**(1), 1432 (2022).
22. Y. Cao, W. Jin, L. H. Ho, and Z. Liu, "Evanescent-wave photoacoustic spectroscopy with optical micro/nano fibers," *Opt. Lett.* **37**(2), 214–216 (2012).
23. Y. He, Y. Ma, Y. Tong, X. Yu, Z. Peng, J. Gao, and F. K. Tittel, "Long distance, distributed gas sensing based on micro-nano fiber evanescent wave quartz-enhanced photoacoustic spectroscopy," *Appl. Phys. Lett.* **111**(24), 241102 (2017).
24. Z. Li, Z. Wang, Y. Qi, W. Jin, and W. Ren, "Improved evanescent-wave quartz-enhanced photoacoustic CO sensor using an optical fiber taper," *Sens. Actuators, B* **248**, 1023–1028 (2017).
25. K. Liu, T. G. Liu, G. D. Peng, J. F. Jiang, H. X. Zhang, D. G. Jia, Y. Wang, W. C. Jing, and Y. M. Zhang, "Theoretical investigation of an optical fiber amplifier loop for intra-cavity and ring-down cavity gas sensing," *Sens. Actuators, B* **146**(1), 116–121 (2010).
26. L. Tong, J. Lou, and E. Mazur, "Single-mode guiding properties of subwavelength-diameter silica and silicon wire waveguides," *Opt. Express* **12**(6), 1025–1035 (2004).
27. J. Hoffman, S. Ravets, J. Grover, P. Solano, P. Kordell, J. Wong-Campos, L. Orozco, and S. Rolston, "Ultrahigh transmission optical nanofibers," *AIP Adv.* **4**(6), 067124 (2014).
28. T. A. Birks and Y. W. Li, "The shape of fiber tapers," *J. Lightwave Technol.* **10**(4), 432–438 (1992).
29. Q. Wang, J. Chang, F. P. Wang, and W. Wei, "Recovery of pure wavelength modulation second harmonic signal waveforms in distributed feedback diode laser-based photoacoustic spectroscopy," *Sens. Actuators, A* **245**, 54–62 (2016).
30. P. Zhimin, D. Yanjun, C. Lu, L. Xiaohang, and Z. Kangjie, "Calibration-free wavelength modulated TDLAS under high absorbance conditions," *Opt. Express* **19**(23), 23104–23110 (2011).
31. Y. Peng, W. Zhang, L. Li, and Q. Yu, "Tunable fiber laser and fiber amplifier based photoacoustic spectrometer for trace gas detection," *Spectrochim. Acta, Part A* **74**(4), 924–927 (2009).
32. M. Hu, M. Hu, W. Wang, and Q. Wang, "Wavelength-scanned all-fiber cavity ring-down gas sensing using an L-band active fiber loop," *Appl. Phys. B* **128**(2), 30 (2022).
33. D. C. Song, J. L. Zou, Z. X. Wei, S. M. Yang, and H. L. Cui, "High-sensitivity fiber Bragg grating pressure sensor using metal bellows," *Opt. Eng.* **48**(3), 034403 (2009).
34. S. Schilt and L. Thevenaz, "Wavelength modulation photoacoustic spectroscopy: Theoretical description and experimental results," *Infrared Phys. Technol.* **48**(2), 154–162 (2006).

35. M. Guo, K. Chen, B. Yang, C. Li, B. Zhang, Y. Yang, Y. Wang, C. Li, Z. Gong, and F. Ma, "Ultrahigh Sensitivity Fiber-Optic Fabry-Perot Interferometric Acoustic Sensor Based on Silicon Cantilever," *IEEE Trans. Instrum. Meas.* **70**, 1–8 (2021).
36. X. Yin, L. Dong, H. Wu, H. Zheng, W. Ma, L. Zhang, W. Yin, S. Jia, and F. K. Tittel, "Sub-ppb nitrogen dioxide detection with a large linear dynamic range by use of a differential photoacoustic cell and a 3.5 W blue multimode diode laser," *Sens. Actuators, B* **247**, 329–335 (2017).
37. J. Wo and Q. Sun, "Theoretical and experimental investigation of multi-wavelength fiber laser," in *Photonics and Optoelectronics Meetings (POEM) 2009: Fiber Optic Communication and Sensors* (SPIE, 2009), 359–365.
38. K. Liu, W. C. Jing, G. D. Peng, J. Z. Zhang, D. G. Jia, H. X. Zhang, and Y. M. Zhang, "Investigation of PZT driven tunable optical filter nonlinearity using FBG optical fiber sensing system," *Opt. Commun.* **281**(12), 3286–3290 (2008).
39. Q. Wang, Z. Wang, and W. Ren, "Wavelength-stabilization-based photoacoustic spectroscopy for methane detection," *Meas. Sci. Technol.* **28**(6), 065102 (2017).
40. G. Ping, X. Liang, Q. Q. Xiao, and W. Rui, "A QEPAS-Based Central Wavelength Stabilized Diode Laser for Gas Sensing," *IEEE Photon. Technol. Lett.* **27**(5), 545–548 (2015).